Available online at www.sciencedirect.com
ScienceDirect
Trans. Nonferrous Met. Soc. China 29(2019) 2556−2565
Transactions of Nonferrous Metals Society of China
www.tnmsc.cn

Effect of Si and Ti on dynamic recrystallization of high-performance Cu−15Ni−8Sn alloy during hot deformation

Chao ZHAO[1], Zhi WANG[1,2], De-qing PAN[1], Dao-xi LI[1], Zong-qiang LUO[1,2], Da-tong ZHANG[1,2], Chao YANG[1,2], Wei-wen ZHANG[1,2]

1. Guangdong Key Laboratory for Processing and Forming of Advanced Metallic Materials, South China University of Technology, Guangzhou 510640, China;
2. School of Mechanical and Automotive Engineering, South China University of Technology, Guangzhou 510640, China

Received 11 March 2019; accepted 3 July 2019

Abstract: Effect of Si and Ti on dynamic recrystallization (DRX) of Cu−15Ni−8Sn alloy was studied using hot compression tests over deformation temperature range of 750−950 °C and strain rate range of 0.001−10 s^{-1}. The results show that the dynamic recrystallization behavior during hot deformation is significantly affected by the trace elements of Si and Ti. The addition of Si and Ti promotes the formation of $Ni_{16}Si_7Ti_6$ particles during hot deformation, which promotes the nucleation of dynamic recrystallization by accelerating the transition from low-angle boundaries (LABs) to high-angle boundaries (HABs). $Ni_{16}Si_7Ti_6$ particles further inhibit the growth of recrystallized grains through the pinning effect. Based on the dynamic recrystallization behavior, a processing map of the alloy is built up to obtain the optimal processing parameters. Guided by the processing map, a hot-extruded Cu−15Ni−8Sn alloy with a fine-grained microstructure is obtained, which shows excellent elongation of 30% and ultimate tensile strength of 910 MPa.
Key words: Cu−15Ni−8Sn alloy; discontinuous dynamic recrystallization; hot compression; hot extrusion; mechanical properties

1 Introduction

Cu−15Ni−8Sn alloys possess outstanding strength, corrosion resistance and wear resistance, which have strong prospects as high-performance bearings and highly wear-resistant components for aerospace and mechanical systems [1,2]. However, the as-cast Cu−15Ni−8Sn alloy ingots usually possess poor ductility owing to the inevitable casting defects, such as slag inclusions and porosities [3,4]. Therefore, additional processes such as plastic deformation (e.g., hot rolling, forging and extrusion) and subsequently heat treatments (e.g. solid solutionizing and annealing) are required to relieve the residual stress and improve the mechanical properties [5,6]. It is known that the above-mentioned casting defects can be effectively reduced by secondary process of hot extrusion [7,8]. Furthermore, dynamic recrystallization can occur during hot extrusion, thus resulting in grain refinement and hence a significant enhancement of the mechanical properties [9−11]. Therefore, it is possible to achieve high strength and good plasticity for the as-extruded Cu−15Ni−8Sn alloy by carefully tuning the dynamic recrystallization behavior, where no additional heat treatment is required.

Many previous studies were focused on the enhancement of strength of aged Cu−15Ni−8Sn alloys by adding trace elements such as Si and Ti, indicating that these additions can effectively retard the migration of grain boundaries and dislocations during heat treatment by the formation of finely dispersed insoluble particles [12,13]. The effects of these fine particles on grain boundaries may favorably adjust the dynamic recrystallization behavior during thermal deformation and thus improve the mechanical properties [14,15]. However, the effect of Si and Ti on the dynamic recrystallization in Cu−15Ni−8Sn alloy has been very rarely reported. In this work, a comprehensive study on the hot deformation behavior of the Cu−15Ni−8Sn alloy with the minor additions of Si and Ti was carried out and a high-performance Cu−15Ni−8Sn alloy was developed through hot extrusion without heat treatment process.

Foundation item: Project (2015A030312003) supported by the Guangdong Natural Science Foundation for Research Team, China
Corresponding author: Wei-wen ZHANG; Tel: +86-20-87112022; E-mail: mewzhang@scut.edu.cn
DOI: 10.1016/S1003-6326(19)65163-0

2 Experimental

In the present study, a Cu−15Ni−8Sn−0.3Si−0.1Ti (wt.%) alloy ingot was prepared in an intermediate frequency induction furnace. The chemical composition of the ingot is given in Table 1. The cast ingot was homogenized at 840 °C for 8 h and subsequently cut into *d*8 mm × 12 mm cylindrical compression specimens. Figure 1 shows the initial microstructure of the as-cast and homogenized materials. These specimens were compressed to a final true strain of 0.9 at 750, 800, 850, 900 and 950 °C with strain rates of 10^{-3}, 10^{-2}, 10^{-1}, 1 and 10 s^{-1} on a Gleeble−3500 thermal simulator. In order to obtain detailed information of early deformation processes, specimens were deformed to a true strain of 0.15, with a strain rate of 1×10^{-3} at deformation temperatures of 750, 850 and 950 °C, respectively. The deformed specimens were water-quenched immediately to room temperature and then sectioned along the compression direction.

Table 1 Chemical compositions of alloy (wt.%)

Ni	Sn	Si	Ti	Cu
15.23	7.92	0.29	0.09	Bal.

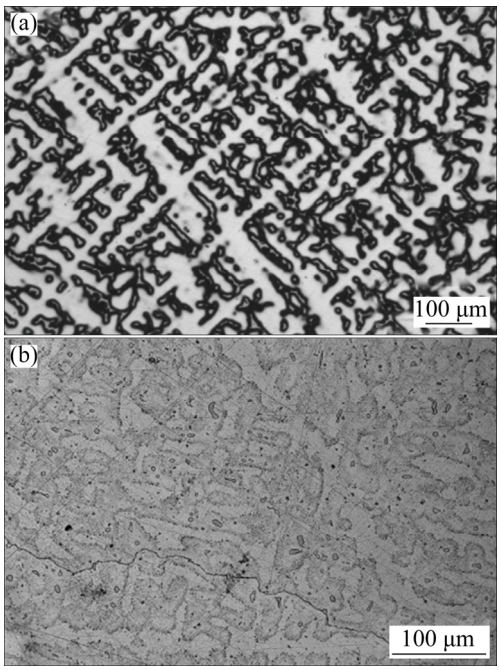

Fig. 1 Optical micrographs of Cu−15Ni−8Sn−0.3Si−0.1Ti alloy in as-cast (a) and homogenized (b) conditions

Extrusion bars were prepared on a vertical extruding machine. Both the diameter and length of the billets were 50 mm. The extrusion parameters, such as extrusion temperature, extrusion ratio and ram speed, were optimized based on the hot processing maps and microstructure evolution. The ingot and extrusion bars were cut into cylindrical tensile samples with a gauge section of 5 mm in diameter and 25 mm in length according to the Chinese GB/T 228−2002 standards. Tensile tests were performed on an Instron 5569 testing machine.

Microstructural evolution was illustrated with a LEICA/DMI 5000M optical microscope (OM) and a FEI NONA430 scanning electron microscope (SEM) equipped with electron backscatter diffraction (EBSD). Specimens for OM and SEM observation were prepared by polishing and then etching in a solution of $FeCl_3$ (5 g) + HCl (10 mL) + H_2O (100 mL). Samples for EBSD measurements were electropolished in a 50% solution of phosphoric acid at 6.5 V for 60 s. Transmission electron microscope (TEM) observation was performed on a FEI TECNAI G2 S-TWIN F20. TEM samples were prepared with twin-jet electro-polishing method in 95% alcohol and 5% perchloric acid at −20 °C.

3 Results and discussion

3.1 Hot deformation behavior of Cu−15Ni−8Sn−0.3Si−0.1Ti alloy

Figure 2 depicts the true stress−strain curves derived from hot compression tests. The flow behavior of the alloy is strongly affected by deformation temperature and strain rate. Under a certain strain rate, the flow stress decreases with increasing deformation temperature, whereas the flow stress increases with increasing strain rate at a prescribed deformation temperature. Typical dynamic recovery (DRV) behavior is observed at low temperatures, for instance, at 750 °C and 1 s^{-1} (Fig. 2(a)). Continuous reduction in the flow stress is observed at strain rates higher than 1 s^{-1}, which is due to the heat accumulation in the specimen during deformation. The typical dynamic recrystallization (DRX) behavior is observed at 950 °C and 0.01 s^{-1} (Fig. 2(b)). A serration is observed on the true stress−strain curves, which may be related to occurrence of dynamic recrystallization [16].

The hot processing map technology based on a dynamic materials model (DMM) is a convenient technique to optimize hot deformation process [17−19]. The theoretical methods for processing maps have been illustrated in detail by PRASAD [20,21]. The total absorbed power (P) of the system can be expressed as

$$P=\sigma\dot{\varepsilon}=G+J=\int_0^{\dot{\varepsilon}}\sigma \mathrm{d}\dot{\varepsilon}+\int_0^{\sigma}\dot{\varepsilon}\mathrm{d}\sigma \quad (1)$$

where σ is the flow stress and $\dot{\varepsilon}$ is the strain rate. G represents the absorbed power dissipated by the rise of temperature, and J represents the power dissipated by microstructure evolution.

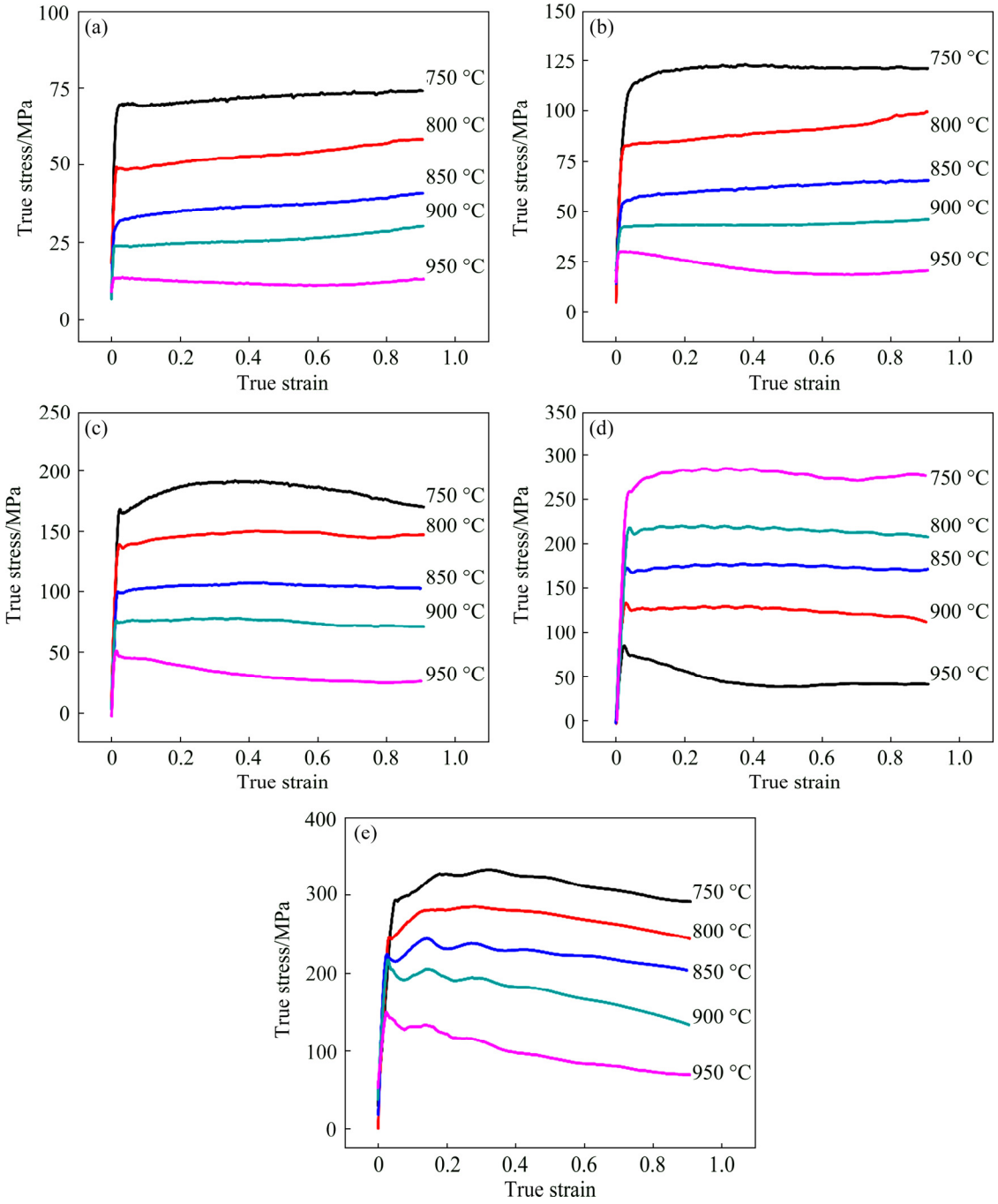

Fig. 2 True stress−strain curves of Cu−15Ni−8Sn−0.3Si−0.1Ti alloy at various strain rates and different deformation temperatures: (a) $\dot{\varepsilon}$ =0.001 s^{-1}; (b) $\dot{\varepsilon}$ =0.01 s^{-1}; (c) $\dot{\varepsilon}$ =0.1 s^{-1}; (d) $\dot{\varepsilon}$ =1 s^{-1}; (e) $\dot{\varepsilon}$ =10 s^{-1}

m is the strain rate sensitivity coefficient, which is related to the change of G and J, as given by

$$m=\left(\frac{\partial(\lg\sigma)}{\partial(\lg\dot{\varepsilon})}\right)_{\varepsilon,T}\approx\frac{\bar{\dot{\varepsilon}}\mathrm{d}\bar{\sigma}}{\bar{\sigma}\mathrm{d}\bar{\dot{\varepsilon}}}=\frac{\mathrm{d}J}{\mathrm{d}G} \tag{2}$$

η represents the efficiency of power dissipation. It can be expressed as

$$\eta=\frac{2m}{m+1} \tag{3}$$

The power dissipated map can be established from η varied with deformation temperature and strain rate. A continuum criterion for the occurrence of flow instability can be obtained by utilizing the principle of maximum rate of entropy production:

$$\xi(\bar{\dot{\varepsilon}})=\frac{\partial\ln[m/(m+1)]}{\partial\ln\bar{\dot{\varepsilon}}}+m\le 0 \tag{4}$$

The variation of $\xi(\bar{\dot{\varepsilon}})$ with deformation temperature and strain rate constitutes the instability map. Finally, the processing map can be established by

superimposing the instability map on the power-dissipation map.

The processing maps of the Cu−15Ni−8Sn−0.3Si−0.1Ti alloy deformed at strains of 0.3, 0.6 and 0.9 were obtained by the above method, which are shown in Fig. 3. In these maps, the contours express the efficiency of power dissipation, and the shaded domains indicate the unsteady zone. The unsteady zone appears at low temperatures and a high strain rate of 0.3 (Fig. 3(a)). As strain increases, the temperature range of unsteady zone increases from 750−800 °C to 750− 900 °C, whereas the efficiency of power dissipation decreases with increasing strain rate. The value of processing efficiency decreases

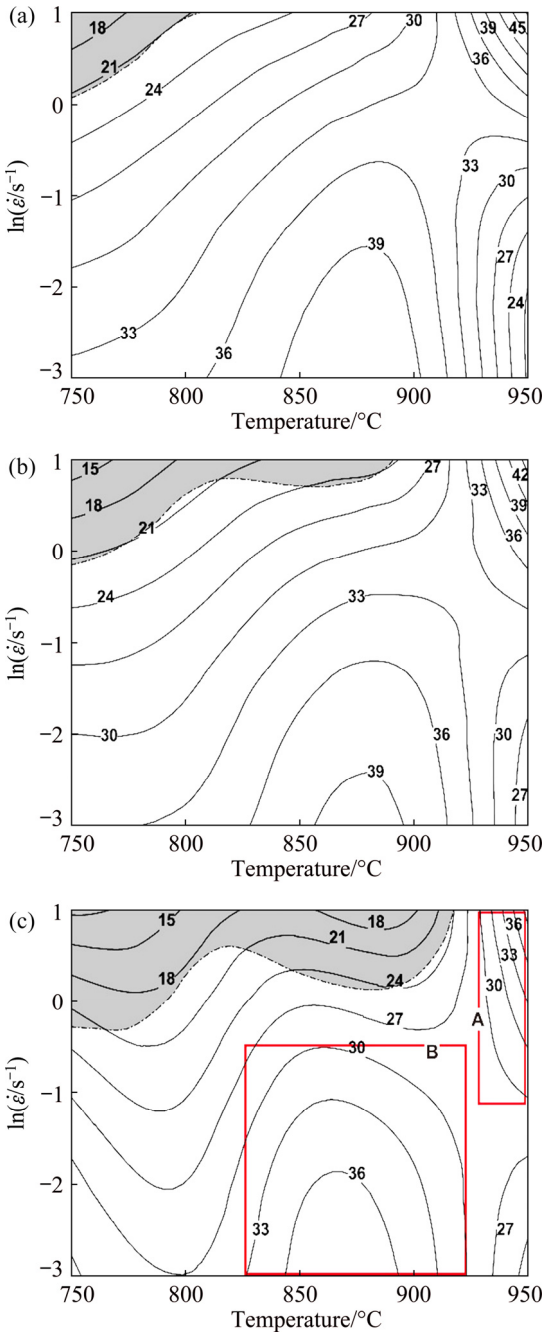

Fig. 3 Processing maps for alloy at different true strains: (a) 0.3; (b) 0.6; (c) 0.9

at high temperatures and low strain rates, which is likely associated with DRX grain coarsening [22]. Generally, a lager dissipation efficiency indicates a better workability of the material [23,24]. The principle of selecting the optimized dissipation efficiency is choosing the relatively higher dissipation efficiency on the premise of avoiding the instability zone. In the processing maps corresponding to a strain of 0.9 (Fig. 3(c)), two relatively higher dissipation efficiency domains are selected. Domain A is in the range of 925−950 °C and strain rate of 1−10 s^{-1}, where the maximum dissipation efficiency is 43% and the minimum dissipation efficiency is more than 27%. Domain B occurs in the range of 825−925 °C and the strain rate range of 1×10^{-3}−0.6 s^{-1}, where the maximum dissipation efficiency is 37% and the minimum dissipation efficiency is also more than 27%. To determine which domain should be the optimum processing window for the Cu−15Ni−8Sn−0.3Si−0.1Ti alloy, the microstructural features and deformation mechanisms are further investigated.

Optical images of Cu−15Ni−8Sn−0.3Si−0.1Ti alloy deformed under different conditions are shown in Fig. 4. The Sn-rich γ particles precipitate from the Cu matrix in the specimens deformed at 750−800 °C, which distribute along the dendrites. Figures 4(a, b) show that the grains are elongated perpendicular to the compression direction. Deformation bands (DBs) are observed around the original grain boundaries. Ultrafine grains nucleate and grow along the DBs, indicating that the DRX preferentially initiates near the DBs [25]. However, γ phase disappears and recrystallization occurs around the original grain boundaries when the deformation temperature is increased to 850−900 °C (Figs. 4(c, d)). The recrystallized grains show a refined structure with a diameter of ~10 μm. The serrated grain boundaries are marked by arrows in Fig. 4(d), confirming occurrence of dynamic recrystallization [26]. Figure 4(f) shows the microstructure of the alloy deformed at 950 °C and 1 s^{-1} in Domain A (marked in Fig. 3(c)), indicating an overheated structure with large-sized grains and coarse second phases. Cracks appear in the specimen under this deformation condition due to a decrease in the binding force of the grain boundaries. Therefore, the optimum processing window should be located in the temperature range from 825 to 925 °C and a strain rate range from 1×10^{-3} to 0.6 s^{-1} (Domain B shown in Fig. 3(c)).

3.2 Dynamic recrystallization of Cu−15Ni−8Sn−0.3Si−0.1Ti alloy

Figure 5 shows the EBSD maps of the specimens deformed with a true strain of 0.9 at a strain rate of 1×10^{-3} s^{-1}. In Figs. 5(a, b), narrow white and bold black lines correspond to boundaries of misorientation $5°<\theta<15°$ and $15°<\theta$, respectively. Only very few

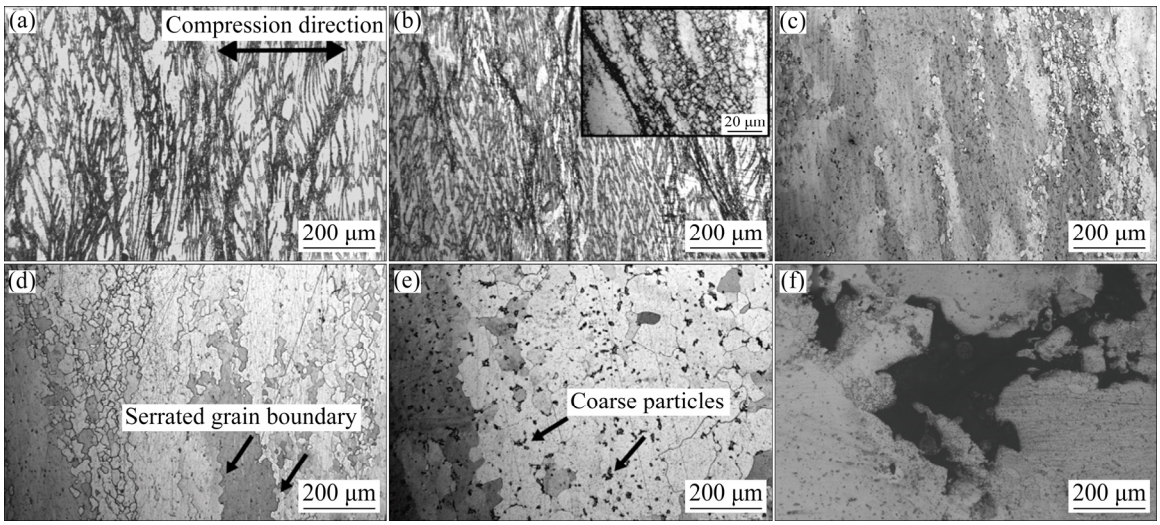

Fig. 4 Optical micrographs of hot compressed specimens with strain of 0.9 under different deformation conditions: (a) 750 °C, 1×10^{-3} s^{-1}; (b) 800 °C, 1×10^{-3} s^{-1}; (c) 850 °C, 1×10^{-3} s^{-1}; (d) 900 °C, 1×10^{-3} s^{-1} (Domain B in Fig. 3(c)); (e) 950 °C, 1×10^{-3} s^{-1}; (f) 950 °C, 1 s^{-1} (Domain A in Fig. 3(c))

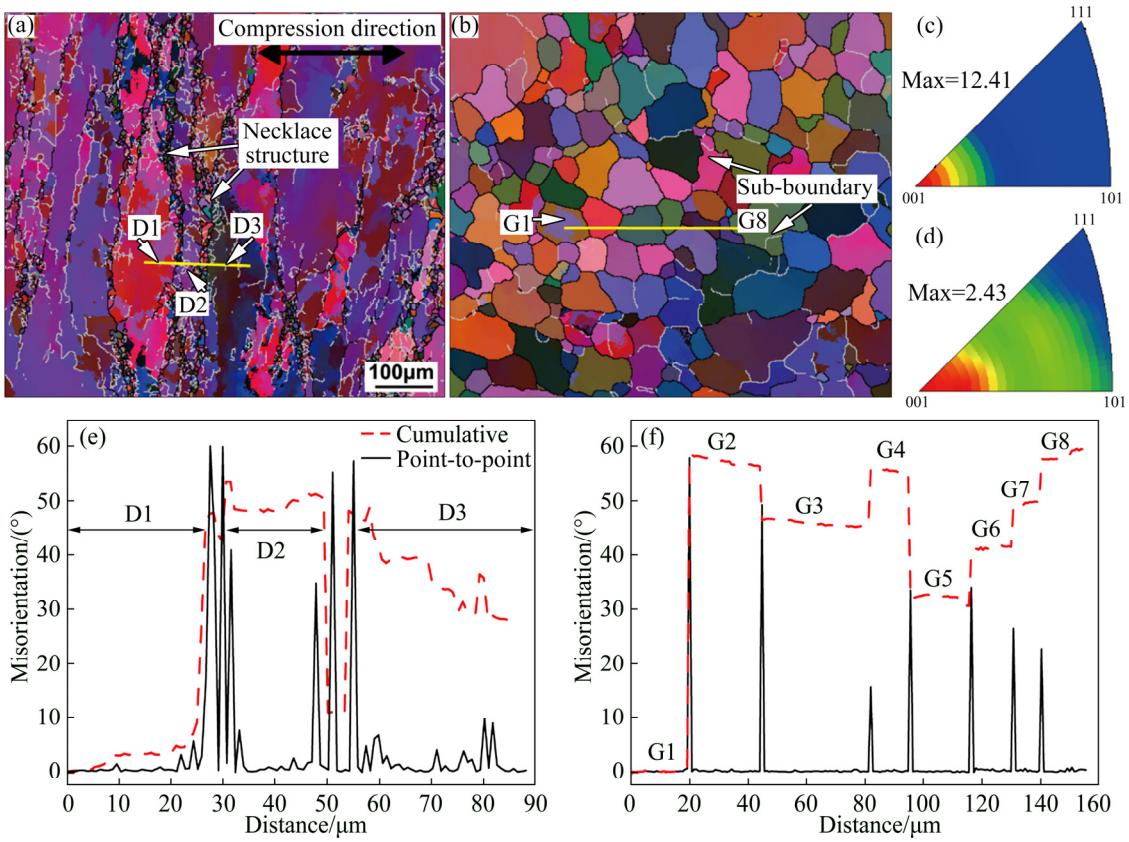

Fig. 5 EBSD micrograph and analysis of designed alloys obtained with true strain of 0.9 at strain rate of 1×10^{-3} s^{-1} at different temperatures: (a, c) 750 °C; (b, d) 950 °C; (e, f) Misorientation measured along lines marked in (a) and (b), respectively

low-angle boundaries (LABs, $5°<\theta<15°$) are observed in the grains, indicating that full DRX occurs at 950 °C (Fig. 5(b)). The texture of ⟨001⟩ fibers is observed in the specimen deformed at 750 °C (shown in Fig. 5(c)), which is related to the orientation of deformation of initial grains [27]. The ⟨001⟩ texture decreases when the temperature is increased to 950 °C (Fig. 5(d)), which is contributed to the random orientation of DRX grains. The point-to-point misorientations and cumulative misorientations of the initial grains are shown in Figs. 5(e, f), indicating that misorientations in D1, D2 and D3 domains (Fig. 5(a)) increase from the grain

interior to the grain boundary. Fine DRX grains form around the original grains, which show a typical "necklace" structure (Fig. 5(a)). The gradient of misorientations and formation of "necklace" structure indicate that discontinuous dynamic recrystallization (DDRX) is the main nucleation mechanism of DRX in Cu−15Ni−8Sn−0.3Si−0.1Ti alloys [28,29].

The LABs developing near recrystallized grain boundaries are helpful to form sub-boundaries (see Fig. 5(b)), owing to the plastic accommodation occurring near the recrystallized grain boundaries during hot deformation [30]. Figure 5(f) shows that the point-to-point misorientations in recrystallized grains (G1−G8) can be sustained within 3° and that the cumulative misorientations do not exceed 5°. This result indicates that continuous dynamic recrystallization (CDRX) plays a minor role in the entire deformation process.

Figure 6 presents the TEM observation results of specimens deformed at temperatures of 750 °C and 800 °C and true strains of 0.15 and 0.90. Figure 6(a) shows that at the early stage of the restoration process (ε=0.15), fine particles (30−70 nm) distribute in the Cu matrix. The EDX analysis and the fast Fourier transform (FFT) pattern (Fig. 6(d)) indicate the fine particles as $Ni_{16}Si_7Ti_6$ intermetallic compounds. The interfaces between the $Ni_{16}Si_7Ti_6$ phase and the Cu matrix are continuous and well bonded, as shown in the high-resolution TEM image in Fig. 6(b). Meanwhile, the two-dimensional misfit (insets I and II in Fig. 6(b)) indicates that the interfaces are semi-coherent. Analysis of FFT pattern in Fig. 6(d) reveals that the crystal orientation relationship between the matrix and $Ni_{16}Si_7Ti_6$ precipitate (FCC, cell parameter is 11.19 Å) can be indexed as follows: $[011]_M//[116]_P$, $(11\bar{1})_M // (51\bar{1})_P$ and $(100)_M//(2\bar{2}0)_P$. In addition, γ phases are observed at the early stage of the restoration process (Fig. 6(e)). At the dynamic equilibrium stage of the restoration process (ε=0.9), dislocation walls are observed near the γ phase (Fig. 6(g)), and dislocation accumulation occurs near the larger γ particles (Fig. 6(h)). The high density of dislocations and the formation of dislocation walls at a strain of 0.9 indicate that dynamic recovery is dominant in alloys deformed at 750 and 800 °C.

Figure 7 shows TEM images of the specimens deformed at a strain rate of 1×10^{-3} s^{-1} and temperatures of 850 and 900 °C and true strains of 0.15 and 0.9. The $Ni_{16}Si_7Ti_6$ particles are observed in specimen obtained at a strain of 0.15 and a deformation temperature of 850 °C (Fig. 7(a)). The average size of the precipitates (~200 nm) is larger than that of the specimen deformed at 750 °C (~50 nm). Dislocation walls form at a strain of 0.15, which is faster than the formation of dislocation walls

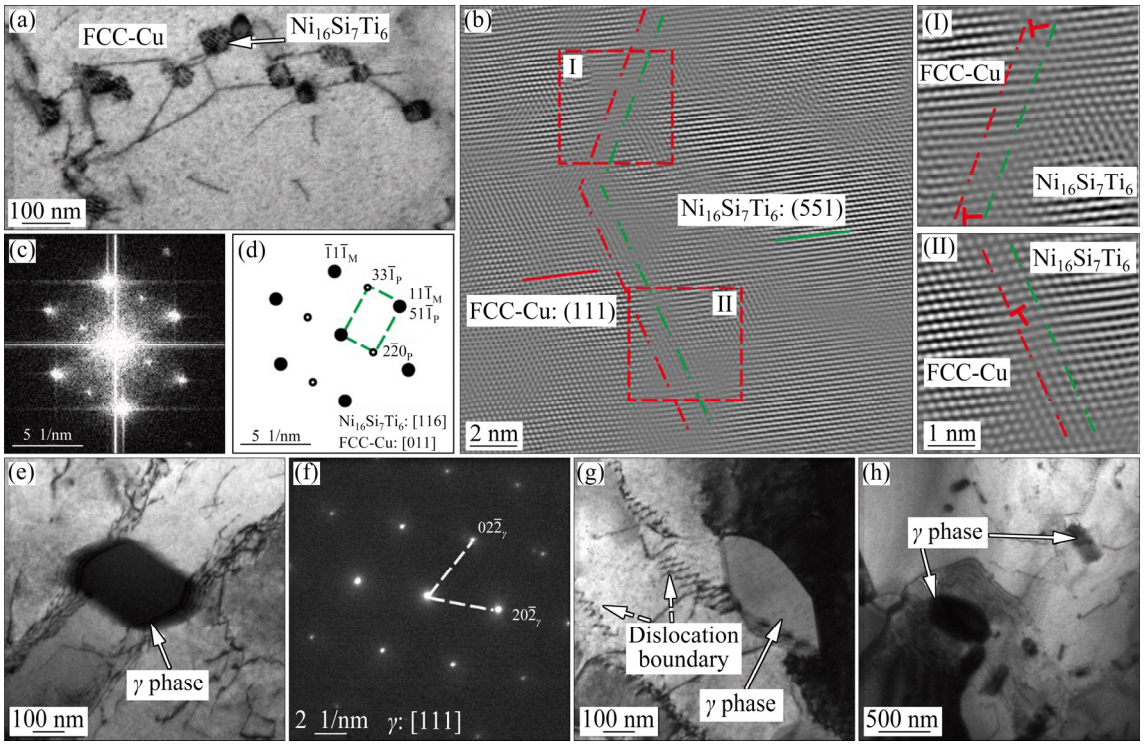

Fig. 6 TEM observation results of hot compressed specimens at strain rate of 1×10^{-3} s^{-1}: (a) TEM image of $Ni_{16}Si_7Ti_6$ particles at 750 °C and ε=0.15; (b) High-resolution TEM (HRTEM) image of boundary between matrix and $Ni_{16}Si_7Ti_6$ particle, along with insets ((I) and (II)) showing close-up images; (c) FFT (fast Fourier transform) pattern of (b); (d) Schematic of pattern in (c); (e) TEM image of γ phase at 750 °C and ε=0.15; (f) Selected-area diffraction pattern (SADP) of γ phase in (e); (g, h) TEM images of specimen deformed with ε=0.90, at 750 and 800 °C, respectively

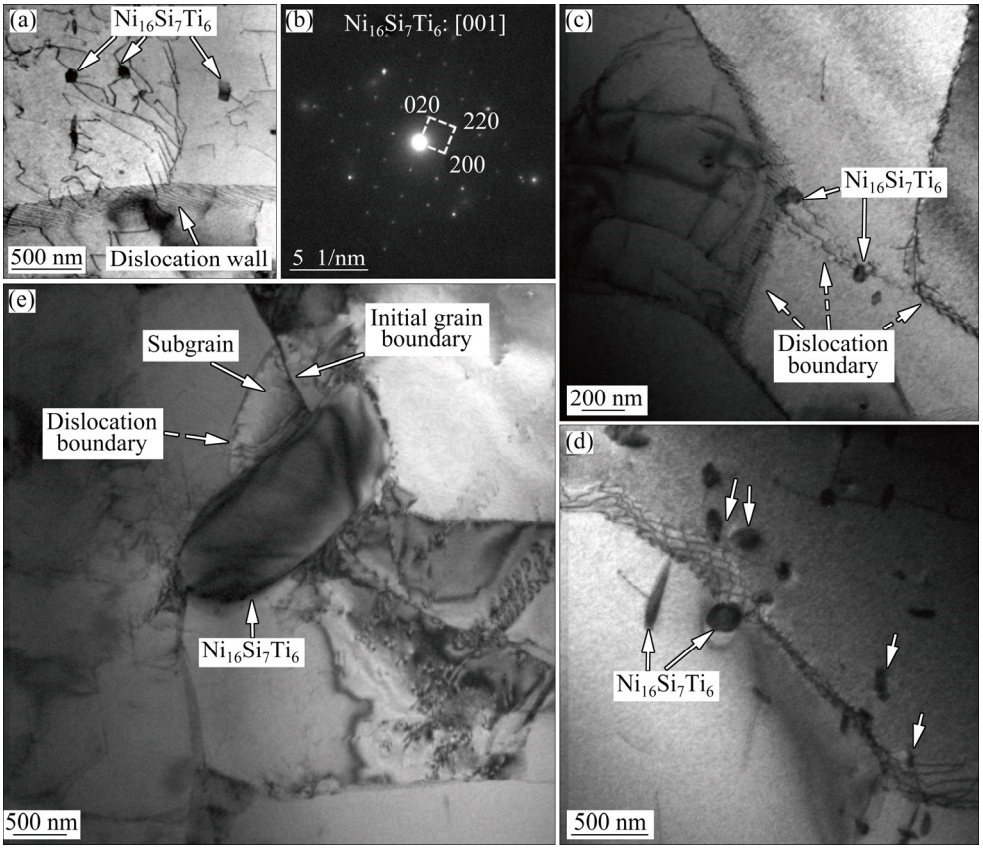

Fig. 7 Microstructure and phases of alloy with strain rate of 1×10^{-3} s^{-1}: (a) TEM image of $Ni_{16}Si_7Ti_6$ particles at 850 °C and ε=0.15; (b) Selected-area diffraction pattern (SADP) of $Ni_{16}Si_7Ti_6$ particle in (a); (c, d) TEM images of $Ni_{16}Si_7Ti_6$ particles and dislocation boundaries at 850 °C and ε=0.90; (e) Subgrain in vicinity of $Ni_{16}Si_7Ti_6$ particle at 900 °C and ε=0.90

at 750 °C. Meanwhile, no γ phase is observed in the specimen. As the true strain is increased to 0.9, the dislocations of two or more Burgers vectors react to form two-dimensional dislocation boundaries (Fig. 7(d)). Figure 7(c) indicates that subgrain boundaries form by the dislocation boundaries at 850 °C. Some subgrains are observed in the area surrounded by the initial grain boundary, the larger-size $Ni_{16}Si_7Ti_6$ particle and the dislocation boundary (Fig. 7(e)). The appearance of subgrains and the decrease in dislocation density signify the initial stage of DRX. When the alloy is deformed at 850−900 °C, the softening mechanism can be explained by the interaction between DRX and DRV.

Figure 8 shows TEM micrographs of specimens obtained at 950 °C and 1×10^{-3} s^{-1} with true strains of 0.15 and 0.9. As shown in Fig. 8(a), a square network forms from screw dislocations of orthogonal Burgers vectors at a true strain of 0.15. The amount of nanoscale $Ni_{16}Si_7Ti_6$ particles is substantially reduced in the specimens deformed at 950 °C compared with the amount formed at lower deformation temperatures. As the true strain is increased to 0.9, the dislocations already transform into new sub-boundaries at the recrystallized grain boundaries (Fig. 8(b)), which is consistent with the conclusions from EBSD. The dislocation sub-boundaries further indicate that DDRX is the main nucleation mechanism of DRX in the Cu−15Ni−8Sn−0.3Si−0.1Ti alloy [31]. Since the nucleation of DRX occurs near the recrystallized grain boundaries, nanoscale DRX grains are observed in specimen obtained at true strain of 0.9.

Precipitations have a strong impact on DRV and DRX processes. During the DRV process, the hard $Ni_{16}Si_7Ti_6$ particles and γ phases exhibit a strong pinning effect on individual dislocations and thus inhibit the annihilation and rearrangement of dislocations. The LABs are inclined to form near precipitations due to dislocation accumulation (Fig. 6(g)). At the second stage of the restoration process, fine $Ni_{16}Si_7Ti_6$ particles promote the nucleation of DRX owing to the acceleration of the transition from LABs to high-angle boundaries (HABs). The misorientation across the dislocation boundary (θ) of the dislocation walls can be expressed as follows [28]:

$$\theta \approx b/h \tag{5}$$

where b is the magnitude of Burgers vector and h is the spacing of the dislocations.

Because of the pinning effect of $Ni_{16}Si_7Ti_6$ particles

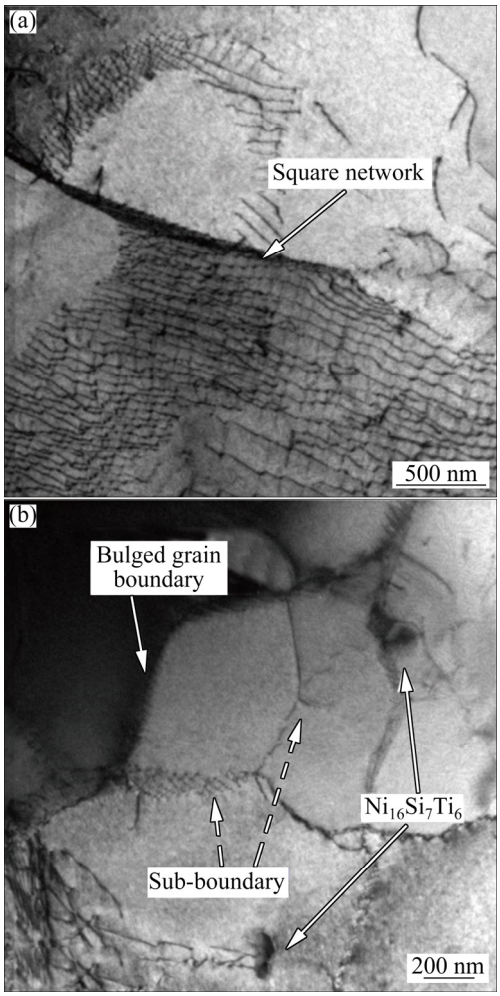

Fig. 8 TEM micrographs of hot compressed specimens obtained at temperature of 950 °C and strain rate of 1×10^{-3} s^{-1} at different true strains: (a) ε=0.15; (b) ε=0.90

on the dislocations, the spacing of the dislocations is decreased. According to Eq. (5), these dislocation walls (LABs), which are close to fine $Ni_{16}Si_7Ti_6$ particles, are more likely to form HABs. As shown in Fig. 7(d), the complex two-dimensional dislocation walls are therefore prone to form in the vicinity of fine $Ni_{16}Si_7Ti_6$ particles. When $Ni_{16}Si_7Ti_6$ particles are located near HABs, LABs are able to interact with these HABs (Fig. 7(c)). As a result, new recrystallized grains are prone to nucleate at these positions. Therefore, $Ni_{16}Si_7Ti_6$ particles promote the nucleation of DRX. For the larger $Ni_{16}Si_7Ti_6$ particles, particle-stimulated nucleation (PSN) of recrystallization is observed (Fig. 7(e)). In the process of deformation, a high density of dislocations form, and particle deformation zones form around the $Ni_{16}Si_7Ti_6$ particles. The particle deformation zone provides both the driving force and position of recrystallization nucleation [31].

At the later stage of the restoration process, DRX can occur in the recrystallized grains with the increase of strain (Fig. 5(b)). The fine particles have the same effects on promoting the nucleation of DRX. They accelerate dislocation accumulation near the recrystallized grain boundaries (Fig. 8(b)). They also exert a pinning effect on both low- and high-angle grain boundaries in the process of DRX grain growth. As a result, it would be easier to maintain the fine and equiaxed DRX grains due to the formation of fine $Ni_{16}Si_7Ti_6$ particles.

3.3 Mechanical properties of hot extruded Cu−15Ni−8Sn−0.3Si−0.1Ti alloy

Hot-extruded alloy with potentially superior mechanical properties has been obtained based on the above processing map and recrystallization behavior analysis. Hot extrusion experiment was performed at a temperature of 900 °C and the extrusion ratio of 17:1 Extruded bars with 500 mm in length and 12 mm in diameter were obtained, which has a smooth surface without any crack. Figure 9 shows the microstructure of the as-extruded sample. Compared to the initial microstructure (shown in Fig. 1), a fine and uniform microstructure is successfully obtained by employing suitable hot deformation and no initial coarse grains are observed, which may effectively contribute to a great improvement of mechanical properties, especially ductility. Size and distribution of $Ni_{16}Si_7Ti_6$ particles are in accordance with results of the hot compressed sample.

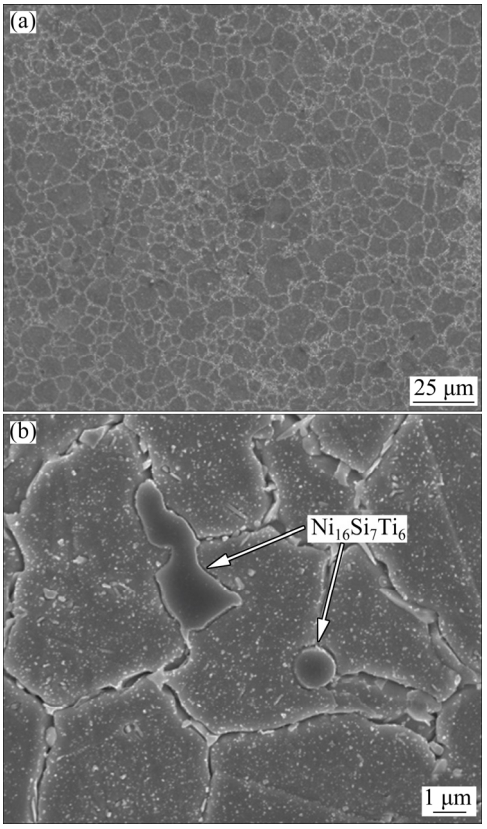

Fig. 9 Cross section microstructures of extruded bar: (a) SEM image of uniform microstructure; (b) SEM image of intergranular $Ni_{16}Si_7Ti_6$ particles

Table 2 gives the mechanical properties of different Cu−15Ni−8Sn alloys. The hot-extruded alloy produced in this study possesses the excellent elongation of 30%, which is higher than the conventional Cu−15Ni−8Sn rod products. The studied alloy also possesses high tensile strength (~910 MPa). Compared with the conventional Cu−15Ni−8Sn products (Table 2), the fine-grained microstructure in the as-extruded sample effectively leads to a great improvement of ductility and simultaneously enhances the strength by grain boundary strengthening [32]. Meanwhile, the ductility can also be increased by eliminating the discontinuous precipitation which otherwise leads to poor ductility. This result illustrates that Cu−15Ni−8Sn−0.3Si−0.1Ti alloy can possess excellent combination of strength and ductility without additional heat treatments by controlling the recrystallization behavior during hot deformation process.

Table 2 Mechanical properties of Cu−15Ni−8Sn alloys

Alloy	State	UTS/MPa	δ/%	Source
Cu−15Ni−8Sn−0.3Si−0.1Ti	Extruded	910	30	This work
Cu−15Ni−8Sn (C96900)	Cast + Spinodally hardened	<758	<4	ASTM B505M-12
Cu−15Ni−8Sn (C72900)	Wrought + Spinodally hardened	825−1035	<15	ASTM B929-05

4 Conclusions

(1) The additions of Si and Ti promote the nucleation of DRX grains due to the formation of $Ni_{16}Si_7Ti_6$ particles that accelerate the transition from LABs to HABs and inhibit the growth of DRX grains through pinning effect.

(2) By controlling the recrystallization behavior, high-performance alloy with ultimate tensile strength of 910 MPa and elongation of 30% is obtained.

(3) DDRX is the main nucleation mechanism of DRX in Cu−15Ni−8Sn−0.3Si−0.1Ti alloy. DDRX also occurs in the recrystallized grains in the later stage of deformation, indicating that a finer microstructure can be obtained at a larger strain.

References

[1] CRIBB W R. Copper spinodal alloys for aerospace [J]. Advanced Materials Processes, 2006, 6: 44.

[2] CRIBB W R, RATKA J O. Copper spinodal alloys [J]. Advanced Materials Processes, 2002, 12: 1−4.

[3] PLEWES J T. Method for producing copper based spinodal alloys: US Patent, 4260432 [P]. 1981−04−07.

[4] CRIBB W R, GEDEON M J, GRENSING F C. Performance advances in copper−nickel−tin spinodal alloys [J]. Advanced Materials Processes, 2013, 9: 20−25.

[5] LIU Xuan, HU Wen-yi, LE Qi-chi, ZHANG Zhi-qiang, BAO Lei, CUI Jian-zhong. Microstructures and mechanical properties of high performance Mg−6Gd−3Y−2Nd−0.4Zr alloy by indirect extrusion and aging treatment [J]. Materials Science and Engineering A, 2014, 612: 380−386. https://doi.org/10.1016/j.msea.2014.06.043.

[6] LI R G, NIE J F, HUANG G J, XIN Y C, LIU Q. Development of high-strength magnesium alloys via combined processes of extrusion, rolling and ageing [J]. Scripta Mater, 2011, 64(10): 950−953. https://doi.org/10.1016/j.scriptamat.2011.01.042.

[7] LUO Bao-min, LI Dao-xi, ZHAO Chao, WANG Zhi, LUO Zong-qiang, ZHANG Wen-wei. A low Sn content Cu−Ni−Sn alloy with high strength and good ductility [J]. Materials Science and Engineering A, 2019, 746: 154−161. https://doi.org/10.1016/j.msea.2018.12.120.

[8] HE Wen-xiong, WANG Er-de, HU Lian-xi, YU Yang, SUN Hong-fei. Effect of extrusion on microstructure and properties of a submicron crystalline Cu−5wt.%Cr alloy [J]. Journal of Materials Processing Technology, 2008, 208(1−3): 205−210. https://doi.org/10.1016/j.jmatprotec. 2007.12.107.

[9] YU Zi-jian, HUANG Yuan-ding, GAN Wei-min, ZHONG Zheng-ye, NORBERT H, MENG Jian. Effects of extrusion ratio and annealing treatment on the mechanical properties and microstructure of a Mg−11Gd−4.5Y−1Nd−1.5Zn−0.5Zr (wt%) alloy [J]. Journal of Materials Science, 2017, 52(11): 6670−6686. https://doi.org/10.1007/s10853-017-0902-3.

[10] WANG Wei-yi, PAN Qing-lin, SUN Yuan-wei, WANG Xiang-dong, LI An-de, SONG Wen-bo. Study on hot compressive deformation behaviors and corresponding industrial extrusion of as-homogenized Al−7.82Zn−1.96Mg−2.35Cu−0.11Zr alloy [J]. Journal of Materials Science, 2018, 53(16): 11728−11748. https://doi.org/10.1007/s10853-018-2388-z.

[11] OUYANG Yi, GAN, Xue-ping, ZHANG Shi-zhong, LI Zhou, ZHOU Ke-chao, JIANG Ye-xin. Age-hardening behavior and microstructure of Cu−15Ni−8Sn−0.3Nb alloy prepared by powder metallurgy and hot extrusion [J]. Transactions of Nonferrous Metals Society of China, 2017, 27(9): 1947−1955. DOI: 10.1016/S1003-6326(17)60219-X.

[12] WANG Yan-hui, WANG Ming-pu, HONG Bin, LI Zhou. Microstructure and properties of Cu−15Ni−8Sn−0.4Si alloy [J]. Transactions of Nonferrous Metals Society of China, 2003, 13(5): 1051−1055.

[13] ZHAO Chao, ZHANG Wei-wen, Wang Zhi, LI Dao-xi, LUO Zong-qiang, YANG Chao, ZHANG Da-tong. Improving the mechanical properties of Cu−15Ni−8Sn alloys by addition of titanium [J]. Materials, 2017, 10(9): 1038. https://doi.org/10.3390/ma10091038.

[14] MONIKA H, FRANK M, ANNA F, CHRISTOPHE D, PAVEL L. Effect of Ca-addition on dynamic recrystallization of Mg−Zn alloy during hot deformation [J]. Materials Science and Engineering A, 2013, 580: 217−226. https://doi.org/10.1016/j.msea.2013.05.054.

[15] RAABE D. Physical metallurgy [M]. 5th ed. Amsterdam: Elsevier, 2004.

[16] HE Jian-liang, ZHANG Da-tong, ZHANG Wen-wei, QIU Cheng, ZHNAG Wen. Constitutive equation and hot compression deformation behavior of homogenized Al−7.5Zn−1.5Mg−0.2Cu−0.2Zr alloy [J]. Materials, 2017, 10(10): 1193. https://doi.org/10.3390/ma10101193.

[17] RAJPUT S K, CHAUDHARI G P, NATH S K. Characterization of hot deformation behavior of a low carbon steel using processing maps, constitutive equations and Zener−Hollomon parameter [J]. Journal of Materials Processing Technology, 2016, 237: 113−125. https://doi.org/10.1016/j.jmatprotec.2016.06.008.

[18] PADMAVARDHANI D, PRASAD Y V R K. Processing maps for hot working of Cu−Ni−Zn alloys [J]. Journal of Materials Science, 1993, 28(19): 5275−5279. https://doi.org/10.1007/BF00570077.

[19] LI Peng-wei, LI Hui-zhong, HUANG Lan, LIANG Xiao-peng, ZHU Ze-xiao. Characterization of hot deformation behavior of AA2014 forging aluminum alloy using processing map [J]. Transactions of Nonferrous Metals Society of China, 2017, 27(8): 1677−1688. https://doi.org/10.1016/S1003-6326(17)60190-0.

[20] PRASAD Y V R K. Processing maps: A status report [J]. Journal of Materials Engineering and Performance, 2003, 22(10): 2867−2874. https://doi.org/10.1007/s11665-013-0732-7.

[21] PRASAD Y V R K, GEGEL H L, DORAIVELU S M, MALAS J C, MORGAN J T, LARK K A, BARKER D R. Modeling of dynamic material behavior in hot deformation-forging of Ti-6242 [J]. Metallurgical Transactions A, 1984, 15(10): 1883−1892. https://doi.org/10.1007/BF02664902.

[22] WANG L, LIU F, CHENG J J, ZUO Q, CHEN C F. Hot deformation characteristics and processing map analysis for nickel-based corrosion resistant alloy [J]. Journal of Alloys and Compounds, 2015, 623: 69−78. http://dx.doi.org/10.1016/j.jallcom.2014.10.034.

[23] CHEN Xi-hong, FAN Cai-he, HU Ze-yi, YANG Jian-jun, GAO Wen-li. Flow stress and dynamic recrystallization behavior of Al−9Mg−1.1Li−0.5Mn alloy during hot compression process [J]. Transactions of Nonferrous Metals Society of China, 2018, 28(12): 2401−2409. https://doi.org/10.1016/S1003-6326(18)64886-1.

[24] FAN Cai-he, PENG Ying-biao, YANG Hai-tang, ZHOU Wei, YAN Hong-ge. Hot deformation behavior of Al−9.0Mg−0.5Mn−0.1Ti alloy based on processing maps [J]. Transactions of Nonferrous Metals Society of China, 2017, 27(2): 289−297. https://doi.org/10.1016/S1003-6326(17)60033-5.

[25] KAI Xi-zhou, CHEN Cun, SUN Xia-fei, WANG Chun-mei, ZHAO Yu-tao. Hot deformation behavior and optimization of processing parameters of a typical high-strength Al−Mg−Si alloy [J]. Materials Design, 2016, 90: 1151−1158. https://doi.org/10.1016/j.matdes.2015.11.064.

[26] ZHANG Hui, ZHANG Hong-gang, PENG Da-shu. Hot deformation behavior of KFC copper alloy during compression at elevated temperatures [J]. Transactions of Nonferrous Metals Society of China, 2006, 16(3): 562−566. https://doi.org/10.1016/S1003-6326(06)60098-8.

[27] WUSATOWSKA-SARNEK A M, MIURA H, SAKAI T. Nucleation and microtexture development under dynamic recrystallization of copper [J]. Materials Science and Engineering A, 2002, 323(1−2): 177−186. https://doi.org/10.1016/S0921-5093(01)01336-3.

[28] HUMPHREYS F J, HATHERLY M. Recrystallization and related annealing phenomena [M]. 2nd ed. Amsterdam: Elsevier, 2004.

[29] FAN Xiao-guang, ZENG Xiang, YANG He, GAO Peng-fei, MENG Miao, ZUO Rui, LEI Peng-hui. Deformation banding in β working of two-phase TA15 titanium alloy [J]. Transactions of Nonferrous Metals Society of China, 2017, 27(11): 2390−2399. https://doi.org/10.1016/S1003-6326(17)60265-6.

[30] HADADZADEH A, MOKDAD F, WELLS M A, CHEN D L. A new grain orientation spread approach to analyze the dynamic recrystallization behavior of a cast-homogenized Mg−Zn−Zr alloy using electron backscattered diffraction [J]. Materials Science and Engineering A, 2018, 709: 285−289. http://dx.doi.org/10.1016/j.msea.2017.10.062.

[31] XI Tong, YANG Chun-guang, SHAHZAD M B, YANG Ke. Study of the processing map and hot deformation behavior of a Cu-bearing 317 LN austenitic stainless steel [J]. Materials Design, 2015, 87: 303−312. https://doi.org/10.1016/j.matdes.2015.08.011.

[32] TONG Yun-xiang, LI Si-yuan, ZHANG Dian-tao, LI Li, ZHENG Yu-feng. High strength and high electrical conductivity CuMg alloy prepared by cryorolling [J]. Transactions of Nonferrous Metals Society of China, 2019, 29(3): 595−600. https://doi.org/10.1016/S1003-6326(19)64968-X.

Si 和 Ti 对高性能 Cu−15Ni−8Sn 合金在热变形过程中动态再结晶的作用

赵 超[1]，王 智[1,2]，潘德清[1]，李道喜[1]，罗宗强[1,2]，张大童[1,2]，杨 超[1,2]，张卫文[1,2]

1. 华南理工大学 广东省金属新材料制备与成形重点实验室，广州 510640；
2. 华南理工大学 机械与汽车工程学院，广州 510640

摘 要：采用不同变形条件 (变形温度 750~950 °C、应变速率 0.001~10 s^{-1})的热压缩试验研究微量元素 Si 和 Ti 添加对 Cu−15Ni−8Sn 合金动态再结晶的作用。结果表明，添加 Si 和 Ti 对热变形过程中的动态再结晶具有显著的作用。添加的 Si 和 Ti 可以形成 $Ni_{16}Si_7Ti_6$ 相，$Ni_{16}Si_7Ti_6$ 相促进低角度晶界向高角度晶界转变，因此，促进动态再结晶的形核过程；同时，$Ni_{16}Si_7Ti_6$ 相产生的钉扎作用抑制再结晶晶粒的长大。基于动态再结晶行为建立热加工图以优化合金的热变形工艺参数。在最优工艺参数下制备具有细小晶粒组织的热挤压态 Cu−15Ni−8Sn 合金，其伸长率达到 30%，抗拉强度达到 910 MPa。

关键词：Cu−15Ni−8Sn 合金；非连续动态再结晶；热压缩；热挤压；力学性能

(Edited by Bing YANG)